DE GRUYTER Nanophotonics 2021; 10(11): 2859–2873

Research Article

Tie-Jun Huang, Li-Zheng Yin, Jin Zhao and Pu-Kun Liu*

High-order multipoles in all-dielectric metagrating enabling ultralarge-angle light bending with unity efficiency

https://doi.org/10.1515/nanoph-2021-0158
Received April 12, 2021; accepted July 9, 2021;

Abstract: Gradient metasurfaces have been extensively applied in the unprecedented control of light beams over thin optical components. However, these metasurfaces suffer from low efficiency when bending light through large angles and high fabrication demand when it requires fine discretion. In this work, we investigate all-dielectric metagratings based on the generalized Kerker effect induced by interference between Mie-type resonances. It allows extraordinary optical diffraction for beam steering through ultralarge angles. The coupling inside and between the lattices in the metagrating can be used to tune the excited states of the electric and magnetic resonances, including both the fundamental dipoles and high-order multipoles, leading to an ideal asymmetrical scattering pattern that redistributes the energy between the diffraction channels as required. The quadrupole and hexadecapole not only significantly enhance the working efficiency but also enable distinctive possibilities for wave manipulation that cannot be reached by dipoles. Utilizing a thin array of silicon rods, large-angle negative refraction and reflection are realized with almost unity efficiency under both transverse magnetic and transverse electric polarization. Compared with conventional metasurfaces, such an all-dielectric metagrating has the merits of high flexibility, high efficiency, and low fabrication requirements. The coupling and interactions among the multipoles may serve as a foundation for various forms of on-chip optical wave control.

Keywords: beam steering; generalized Kerker effect; high-order multipoles; metagrating; Mie resonances.

1 Introduction

The rapid development of exotic metamaterials has enabled the unprecedented manipulation of electromagnetic waves which cannot be attained by natural materials [1, 2]. Recently, dielectric nanoparticles with low dissipative losses and high permittivity, which support Mie-type resonance, have been developed as favorable candidates for various nanophotonics applications [3–5]. Compared with their metallic counterparts, dielectric nanoparticles can excite a rich range of electric and magnetic multipoles without needing geometries such as split-ring resonators or U-shaped particles [6]. The low losses in combination with the localized multipolar nature can support high-quality resonances with the field increased by several orders of magnitude [7, 8]. In addition, the resonances are sustained inside the dielectric particles [9], unlike resonances for plasmonic structures, which mainly rely on surface modes. These properties produce to a strong light–matter interaction and are promising for nonlinear phenomena [10, 11], Fano resonances [12, 13], sensing [14], guiding [15], spectroscopy [16] and magnetic mirrors [17].

Most importantly, by tuning the shape or geometric parameters of dielectric particles, the interplay among the electric and magnetic multipoles can be used to realize unconventional scattering [3–5]. For instance, by overlapping the electric dipole (ED) and magnetic dipole (MD) with identical values in the spectra, no-backward or no-forward scattering can be achieved [18]. Unidirectional scattering has significant potential in various optical applications [19, 20]. As one of the most promising concepts, Huygens metasurfaces based on the Kerker effect can freely modulate the electromagnetic characteristics with an ultrahigh efficiency [17, 21–30]. By accumulating the gradient changes of periodic elements, the phase difference between ED and MD is able to achieve a full 2π phase shift [25]. The abrupt phase changes induced by Huygens metasurfaces

---

***Corresponding author: Pu-Kun Liu**, State Key Laboratory of Advanced Optical Communication Systems and Networks, Department of Electronics, Peking University, Beijing, 100871, China,
E-mail: pkliu@pku.edu.cn. https://orcid.org/0000-0001-8750-7899
Tie-Jun Huang, Li-Zheng Yin and Jin Zhao, State Key Laboratory of Advanced Optical Communication Systems and Networks, Department of Electronics, Peking University, Beijing, 100871, China

enable intriguing wavefront control, leading to various applications, such as abnormal refraction [22–28], focusing [17, 22–24, 26], absorption [29], and artificial colors [30]. Compared with conventional optical devices, a Huygens metasurface has a high flexibility, a low profile, and a high transmission. However, Huygens metasurfaces also have some limitations. Achieving sufficient spatial resolution for the wavefront control requires fine spatial discretization and elaborate fabrication. The corresponding manufactured resolution has a considerable influence on the working performance of the optical devices. When routing beams through large angles, owing to the intrinsic drawbacks of gradient metasurfaces [31, 32], complex geometric configurations are needed to avoid the dramatic decrease of efficiency [33]. The anomalous refractive angles achieved with Huygens metasurfaces are often smaller than 30° [17, 24–28], which is insufficient for many applications.

Due to diffraction and resonance, gratings can transfer the incident energy into a discrete set of diffraction channels according to the Floquet theory. Under these circumstances, the light is bent through a large angle by the uniform elements, which are not so small as to require an extremely high fabrication resolution. A metasurface adopting the diffraction effect is also known as the metagrating which has advantages on achieving extreme wave manipulation [34–36]. The essential principle for the metagrating is completely suppressing all the unselected diffraction channels using asymmetrical scattering elements. It is still difficult to realize this suppression since each channel is not independently controllable [37]. Recently, it has been shown that the interference between Mie resonances in periodic structures with defined multipolar characteristics is a novel way to form scattering patterns, which is known as the generalized Kerker effect [38]. This designed scattering pattern can be used to choose the diffraction order and eliminate all the unwanted channels. Utilizing simple dielectric grating configurations, some pioneering researchers have achieved anomalous refraction with angles of up to 90° [39–44, 47]. However, there remain several important issues plaguing the development of high-index dielectric metagratings based on the generalized Kerker effect.

First, the influence of the lattice coupling between the periodic nanoparticles is comparable to the effect of the resonance inside an individual element [45, 46]. Therefore, the scattering by periodic structures can be totally different from an isolated lattice (IL) [47]. Some studies also utilize the lattice coupling to overlap the ED and MD spectra, but relevant designs for abnormal wavefront control have not yet been fully investigated [45]. Many other investigations just neglect the influence of lattice coupling [39, 48] or do not discuss it in sufficient detail [40–43]. Second, as well as the fundamental ED and MD, the high-order multipoles offer new possibilities in the generalized Kerker effect for shaping complex scattering patterns [49]. Although some works have recognized the importance of these modes, such as in enhancing the scattering directionality or building magnetic mirrors [47, 50, 51], there is still no method for applying or optimizing high-order multipoles in diffraction selection. In addition, periodic doublet configurations have been employed for improving working performances [41–43]. The inter-particle coupling inside doublets is also important for the generalized Kerker effect, but there are few analytical works on this.

In this work, we analytically investigate the efficient manipulation of waves through large angles, as induced by the generalized Kerker effect inside periodic high-index nanoparticles. Based on the multiple scattering theory, both the simple grating (SG), formed by a single dielectric rod in one period, and the compound grating (CG), formed by a dimer in one period, are investigated in detail. The coupling inside and between the periodic dielectric lattices allows not only EDs and MDs but also high-order multipoles to manipulate waves. With appropriate designs, the scattering by the nanoparticles can be elaborately tailored by tuning the interference between the multipoles, allowing the light energy to be harnessed in both the transmission and reflection diffraction channels. Thus, the high-order multipoles not only help to improve the working performance of the dipoles but also play a dominant role in wave control. They have different features from dipoles, which can increase flexibility and working efficiency. Efficiencies close to 100% for the large-angle negative reflection and refraction of incident waves are specifically demonstrated for both transverse magnetic (TM) and transverse electric (TE) polarization. Thus, these low-loss all-dielectric structures may stimulate the design of compact optical components with a low profile and high efficiency.

2 Theory for the interaction of light with dielectric cylinders

Let us start by considering a one-dimensional (1D) array of rods with a refraction index of 3.5 (approaching that of silicon). As shown in Figure 1a and b, the lattices in the array have one or two dielectric cylinders, denoted as SG or CG, respectively. The period of the lattice is L and cylinders are uniform in the z-direction. For the SG, all the rods have the same radius r. A CG lattice is composed of two cylinders with radiuses r_1 and r_2 and a center-to-center distance d. In the local coordinate system for a specific lattice, the line connecting the two rods has an angle ϕ with respect to the x-axis.

To simplify the derivation, we first consider two-dimensional (2D) scattering cases when a plane wave with incident angle θ impinges on the grating. Realizable three-dimensional (3D) cases are calculated and discussed in the last section. The polarization of the incident waves can be TM or TE when the electric or magnetic field is polarized along the z-axis. Under a polar coordinate (ρ, φ), the scattering fields of an isolated cylinder are expanded into a series of cylindrical harmonics:

$$F = \mathbf{P}^T \cdot \boldsymbol{\sigma}, \tag{1}$$

where $\mathbf{P} = [i^m H_m^{(1)}(k_0\rho)e^{im\varphi}]$ and $\boldsymbol{\sigma} = [\sigma_m]$ are column vectors. F is the E_z or H_z component for TE or TM polarization. $H_m^{(1)}$ is the mth-order Hankel function of the first kind and σ_m is the scattering coefficient of the harmonic of the mth cylinder normalized by $2\lambda/\pi$, where λ is the working wavelength [52]:

$$\sigma_m^{\mathrm{TE}} = \frac{J_m(Nk_0r)J_m'(k_0r) - NJ_m(k_0r)J_m'(Nk_0r)}{NJ_m'(Nk_0r)H_m^{(1)}(k_0r) - J_m(Nk_0r)H_m^{\prime(1)}(k_0r)}, \tag{2a}$$

$$\sigma_m^{\mathrm{TM}} = \frac{NJ_m(Nk_0r)J_m'(k_0r) - J_m(k_0r)J_m'(Nk_0r)}{J_m'(Nk_0r)H_m^{(1)}(k_0r) - NJ_m(Nk_0r)H_m^{\prime(1)}(k_0r)}, \tag{2b}$$

in which J_m is the mth-order Bessel function, J'_m and $H'^{(1)}_m$ are the derivatives of the original functions, N is the refractive index of the rod. Then, the total scattering cross-section σ_{s} of a single rod is the sum of all scattering orders:

$$\sigma_{\mathrm{s}} = \sum_m |\sigma_m|^2, \tag{3}$$

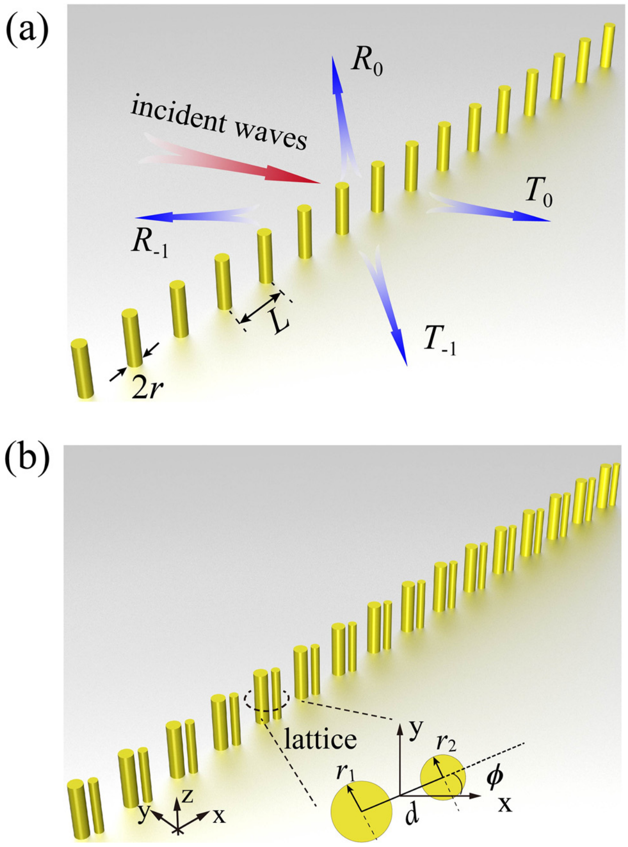

Figure 1: (a) Schematic of an SG formed by a single dielectric rod in one period and (b) presents the structure of CG. The lattice is a doublet. Both gratings are assumed to be infinite in the z-direction.

For TM-polarized waves, $|m| = 0, 1, 2,$ and 3 correspond to the MD, ED, electric quadrupole (EQ), and electric hexadecapole (EH). For TE polarization, $|m| = 0, 1, 2,$ and 3 are the ED, MD, magnetic quadrupole (MQ), and magnetic hexadecapole (MH). The scattering spectra of an isolated silicon rod under the two types of polarization are plotted in Figure S1a and b (Section 1 of the supplementary material). The field distributions and scattering properties of these multipoles are also calculated and illustrated in the supplementary material. It is clear that there are electric and magnetic multipoles under both types of polarization, which enriches the scattering phenomenon of the dielectric rod. The interplay among these multipoles can lead to the generalized Kerker effect. Therefore, it is possible to tailor the excited states of the multipoles through proper geometric design to realize unique scattering properties.

Note that, owing to the rotational symmetry, opposite orders always have the same scattering coefficient and phase difference, i.e., $\sigma_m = \sigma_{-m}$. When the cylinders form a 1D SG, the detailed scattering properties can be analytically investigated by the multiple scattering theory. Thus, the scattering field of an SG can be expressed as [52]:

$$F^{\mathrm{SG}} = \sum_{l=-\infty}^{\infty} \mathbf{P}_l^T \cdot \boldsymbol{\sigma}^{\mathrm{SG}} \mathrm{e}^{-ilk_0L\cos\theta}, \tag{4}$$

Here, $\boldsymbol{\sigma}^{\mathrm{SG}} = [\sigma_m^{\mathrm{SG}}]$ and $\mathbf{P}_l = [H_m^{(1)}(k_0\rho_l)\mathrm{e}^{im\varphi_l}]$ are column vectors. σ_m^{SG} is the unknown scattering coefficient of the mth-order multipole and $\boldsymbol{\rho}_l = [\boldsymbol{\rho} - lL\mathbf{x}] = \rho_l(\mathbf{x}\cos\varphi_l + \mathbf{y}\cos\varphi_l)$. Using the iterative $\mathbf{T}$ matrix [53], the scattering coefficients can be retrieved from:

$$\left(\bar{\mathbf{I}} - \bar{\mathbf{T}} \cdot \bar{\mathbf{C}}\right)\boldsymbol{\sigma}^{SG} = \bar{\mathbf{T}} \cdot \mathbf{B}, \tag{5}$$

where $\mathbf{B} = [(-i)^n \mathrm{e}^{in\theta}]$, $\bar{\mathbf{I}}$ is the unit matrix, $\bar{\mathbf{T}}$ is a diagonal matrix with $T_{mm} = \sigma_m$, and $\bar{\mathbf{C}} = [C_{ml}]$ is the matrix of lattice sum where

$$C_{ml} = \left[\sum_{g=1}^{\infty} H_{m-l}\left(k_o gL\right)\left(\mathrm{e}^{-imk_0 L\cos\theta} + (-1)^{m-l}\mathrm{e}^{imk_0 L\cos\theta}\right)\right], \quad (6)$$

C_{ml} can be calculated by integration. Clearly, the scattering by the cylinders within an SG depends on cylindrical harmonics with coefficient σ_m^{SG}. Note that, the lattice coupling can lead to multipole interactions among the multipoles, so that cylindrical harmonics with opposite signs no longer behave as a whole, i.e., $\sigma_m^{\mathrm{SG}} \neq \sigma_{-m}^{\mathrm{SG}}$.

For the CG, each periodic lattice consists of two dielectric rods. The fields scattered by one rod become the incident waves for the other. Thus, an extra inter-lattice coupling must be considered. To see the influence of this inter-lattice coupling, we first analyze the scattering of an isolated doublet. By considering the multiple couplings and the boundary conditions, the coefficients for the multipoles inside each rod ($\boldsymbol{\sigma}^j = [\sigma_m^j]$ where $j = 1$ or 2 is the number of cylinders) can be found with the following relation:

$$\begin{bmatrix} \boldsymbol{\theta}^1 \\ \boldsymbol{\theta}^2 \end{bmatrix} = \begin{bmatrix} \mathbf{T}_{11} & \mathbf{T}_{12} \\ \mathbf{T}_{21} & \mathbf{T}_{22} \end{bmatrix} \begin{bmatrix} \boldsymbol{\sigma}^1 \\ \boldsymbol{\sigma}^2 \end{bmatrix}, \quad (7)$$

where $\mathbf{T}$ is a square matrix describing the inter-lattice effects, including electric–electric coupling, magnetic–magnetic coupling, and electric–magnetic coupling. For example, T_{12}^{03} characterizes the electric–magnetic coupling between the MD of cylinder 1 and the EH of cylinder 2 under TM polarization. $\boldsymbol{\theta}^j = [\theta_m^j]$ describes the phase shift due to the incident angle and the position of each rod:

$$\theta_m^j = -i^m \mathrm{e}^{ik_0 \frac{d}{2}\cos\left(\phi^j - \theta\right) - im\theta}, \quad (8)$$

where $\phi^j = \phi$ or $-\phi$ for $j = 1$ or 2, representing the angle of the rod center with respect to the x-axis in its local coordinates. After setting the values of the $\mathbf{T}$ matrices (see Section 2 of the supplementary material), $\boldsymbol{\sigma}^j$ can be obtained through Eq. (7). There are more details of the analysis of an IL in the supplementary material.

When the doublet is periodically arranged as a CG, both the inter-lattice coupling and lattice coupling affect the generalized Kerker effect. To characterize the scattering properties quantitatively, each unit cell of the CG is considered to be a single composite structure, such that its scattering features are also described by the multipoles with coefficient $\boldsymbol{\sigma}^{\mathrm{CG}} = [\sigma_m^{\mathrm{CG}}]$. Then, the theoretical derivation for the CG is like that for the SG, except that the $\mathbf{T}$ matrix includes the inter-lattice coupling effect. The $\mathbf{T}$ matrix $\overline{\mathbf{T}} = [\bar{t}_{mn}]$ for CG is

$$\overline{\mathbf{T}} = \overline{\mathbf{T}}_1 \cdot \overline{\boldsymbol{\beta}}_{01} + \overline{\mathbf{T}}_2 \cdot \overline{\boldsymbol{\beta}}_{02}, \quad (9)$$

where $\overline{\mathbf{T}}_1$ and $\overline{\mathbf{T}}_2$ are the $\mathbf{T}$ matrices for each rod for their coordinates, $\overline{\boldsymbol{\beta}}_{01}$ and $\overline{\boldsymbol{\beta}}_{02}$ are the transform matrices between different coordinates. The elements of $\overline{\mathbf{T}}$ describes the coupling effects between two rods in a lattice. The deduction of Eq. (8) and other details of $\overline{\mathbf{T}}$ are put in Section 3 of the supplementary material. The effective scattering coefficient $\boldsymbol{\sigma}^{\mathrm{CG}}$ of a unit cell within the CG can be obtained by substituting the composite $\overline{\mathbf{T}}$ into Eq. (5). It is expected that a more complex scattering behavior will occur for a CG because there is extra coupling inside the composite lattice.

The total transmission and reflection coefficients of the mth-order diffraction harmonics T_m and R_m in Cartesian coordinates are

$$T_m = \left|\delta_{m0} + \frac{2}{L\sqrt{k_{y0}k_{ym}}} \sum_{l=-\infty}^{\infty} \left(-\frac{k_{ym} + ik_{xm}}{k_0}\right)^l \sigma_m^{\mathrm{SG}}\right|^2, \quad (10a)$$

$$R_m = \left|\frac{2}{L\sqrt{k_{y0}k_{ym}}} \sum_{l=-\infty}^{\infty} \left(\frac{k_{ym} - ik_{xm}}{k_0}\right)^l \sigma_m^{\mathrm{SG}}\right|^2, \quad (10b)$$

where $k_{xm} = k_0\cos\theta + m\frac{2\pi}{L}$ and $k_{ym} = \sqrt{k_0^2 - k_{xm}^2}$. The angular radiation pattern of the scattering field is

$$\Phi(\varphi) = \left|\sum_{m=-\infty}^{\infty} \sigma_m^{\mathrm{SG}} \mathrm{e}^{im\left(\frac{\pi}{2}+\varphi\right)}\right|^2, \quad (11)$$

The term σ_m^{SG} in Eqs. (10) and (11) can be replaced by σ_m^{CG} or σ_m to get the corresponding results for a CG or an isolated rod (IR), respectively. The angular scattering shape of an isolated doublet can be calculated with

$$\Phi(\varphi) = \frac{2\lambda}{\pi} \sum_{j=1}^{2} \mathrm{e}^{ik_0\frac{d}{2}\cos\left(\phi^j - \theta\right)} \sum_{m=-\infty}^{\infty} i^n \sigma_m^j \mathrm{e}^{im\theta}, \quad (12)$$

3 Wave steering under TM polarization

As mentioned above, to realize abnormal wave control with extra parameters, the dielectric grating must work in the metagrating regime $L > \lambda/(1 + |\cos\theta|)$. Under this condition, the incident energy is distributed into several discrete channels due to diffraction. Through the generalized Kerker effect induced by the interference between the multipoles, an angular scattering pattern can be generated to control the diffraction. The outgoing waves of the metagrating can be evaluated by multiplying the angular scattering patterns and the directions of the diffraction channels. For the high-efficiency abnormal wave steering, all the diffraction channels must be in the zeros of the angular scattering patterns, except for the T_0 channel and the channel preserved for steering the waves. The T_0 channel cancels out the incoming waves by destructive interference. Then, the incident energy is forced to distribute into the preserved channel, lending to a high-efficiency beam steering. Compared with previous pioneering works that mainly used dipoles [39–43], we aim to improve the working performance and increase the potential of the generalized Kerker effect by considering the contributions of the quadrupole and hexadecapole. The coupling inside and between periodic nanoparticles is employed to tune the states of the multipoles, thus fulfilling the generalized Kerker condition for suppressing unwanted diffraction channels. To show the flexibility of the interference of Mie resonances, both the in-plane negative refraction and reflection induced by the extraordinary optical diffraction are studied as specific examples.

In the metagrating regime, at least four possible diffraction channels are available, i.e., T_0 with $\theta_{T0} = \theta$, T_{-1} with $\theta_{T-1} = \mathrm{arc}\cos(-\lambda/L + \cos(\theta))$, R_0 with $\theta_{R0} = -\theta$, and R_{-1} with $\theta_{R-1} = -\mathrm{arc}\cos(-\lambda/L + \cos(\theta)) - \pi$. The negative refraction under TM polarization when preserving the T_{-1} channel is considered first. We start by considering an SG with $L = 4.3r$ illuminated by a TM-polarized wave at $\lambda = \sqrt{2}L$. The parameters are similar to those in references [41] and [43]. The calculated distribution of $|E|$ is plotted in Figure 2(a1), showing that the channels R_0 and T_0 are totally suppressed. About 20 and 79% of the input energy are distributed into the R_{-1} and T_{-1} channels, resulting in in-plane negative refraction with a 90° bending angle. The multipolar coefficients of a rod inside this SG and an IR are depicted in Figure 2(a2) by red and blue, respectively. Notice that the lattice coupling makes the results for a rod in the SG different from those for the IR. The scattering harmonics with opposite signs no longer behave as a whole, and the coupling of the multipoles has changed the

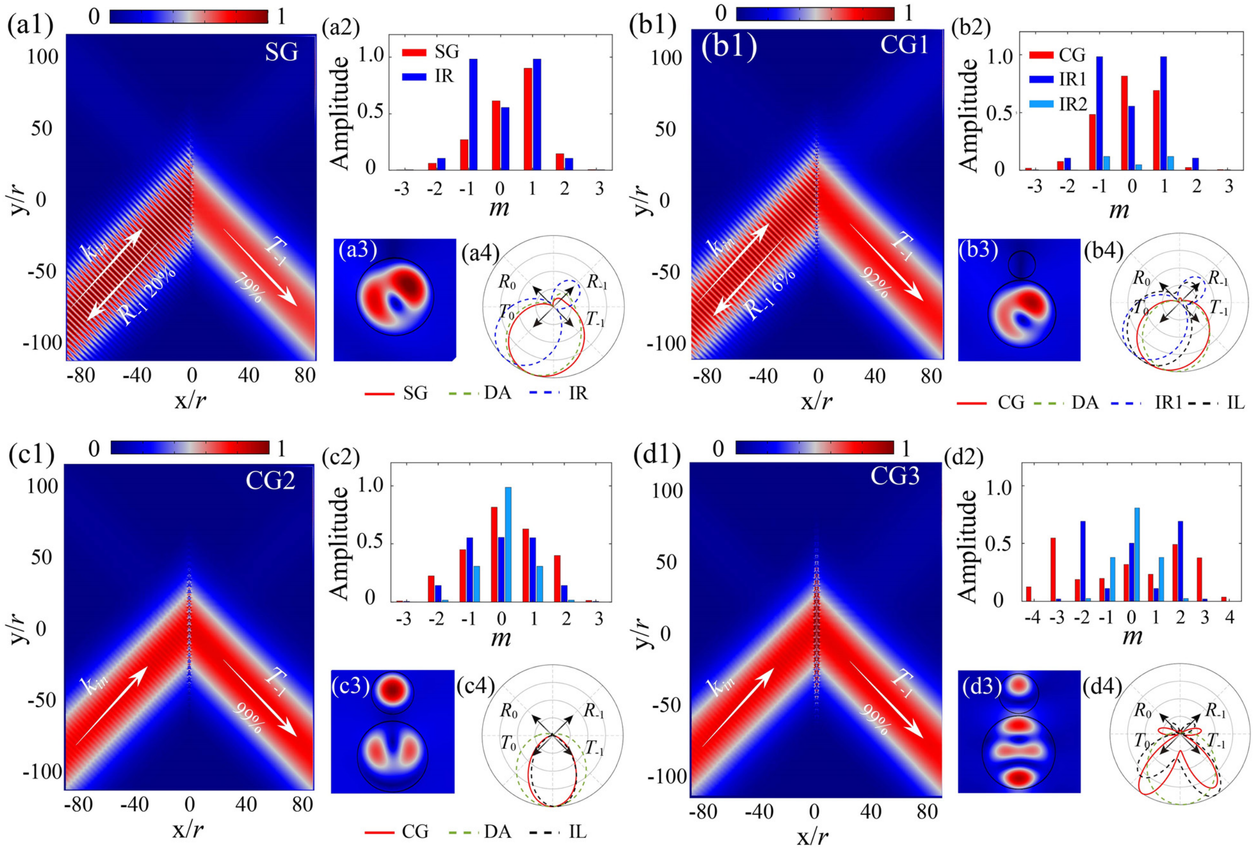

Figure 2: (a)–(d) illustrated the calculated results of SG, CG1, CG2, and CG3, respectively. Numbers '1', '2', '3', and '4' are respectively corresponding to the field distribution of $|E|$ when the rod array is illuminated by a Gaussian beam, the excited coefficients of the cylindrical harmonics, the near-field distribution of $|H|$ and the angular scattering patterns. The scattering pattern of the grating is compared with the approximation of dipoles, the approximation of an isolated rod (SG), and the approximation of an isolated lattice (CG). For all the cases, the period of the grating and the working wavelength are related by $\lambda = \sqrt{2}L$ and $\theta = 45°$, leading to a bending angle of 90°.

exciting amplitude and phase [47]. Clearly, only the dipoles were mainly produced. ED features can be seen in the near-field distribution of $|H|$ in Figure 2(a3). According to the Kerker effect, the interference between dipoles can weaken the backward propagation, which is also visualized by the far-field angular scattering patterns in Figure 2(a4).

As discussed, the cancellation of T_0 is caused by destructive interference between the incident waves and the waves scattered by the cylinders. The angular scattering pattern of each rod is compared with two approximations, the IR approximation and the dipole approximation (DA), for ED + MD, to illustrate the contributions of high-order multipoles and lattice coupling. The importance of lattice coupling for the generalized Kerker effect is obvious as the unique scattering behavior disappears under the IR approximation. However, the DA can reproduce the scattering pattern well, indicating that high-order multipoles do not participate in this steering process. To enhance the working performance, it is necessary to optimize the angular scattering shape by tuning the states of the dipoles or taking high-order multipoles into consideration, but the limited tuning freedom of SG constrains the further improvement.

The extra coupling inside the lattices in a CG provides more possibilities than an SG for the generalized Kerker effect. The first CG (CG1) is also taken from reference [41]. Its parameters are $r_1 = r$, $r_2 = 0.4r$, $d = r_1 + r_2 + 0.05r$, $L = 4.3r$, and $\phi = 90°$. The results, shown in Figure 2(b1)–(b4), indicate a working efficiency of 92%. Unlike the analysis in reference [41], this doublet dimer mainly contributes to enhancing the coefficient of MD rather than the ED. Compared with the SG, the R_{-1} channel is further suppressed due to the enhanced interference between the dipoles. This improvement is induced by the interaction inside the doublet, as shown in Figure 2(b3). However, there are still no high-order multipoles. As above, the far-field scattering pattern of the DA is slightly different from that for CG1. In addition, the scattering pattern of an IL is like that for an IR. Therefore, the negative refraction of CG1 is also mainly caused by lattice coupling.

To take the high-order multipoles into the generalized Kerker effect, one can increase the effective size of the composite unit, which is achieved by increasing the radius of each cylinder or enlarging the separation between them (see Section 2 of the supplementary material). After optimization, a new CG (CG2) is chosen with parameters $r_1 = 1.06r$, $r_2 = 0.64r$, $\phi = 90°$, and $d = r_1 + r_2 + 0.2r$. As illustrated in Figure 2(c1), more than 99% of the incident energy is transferred into the T_{-1} channel. Note that this high-efficiency negative refraction with a bending angle of 90° is hard to realize with common gradient metasurfaces, verifying the advantages of a CG for large-angle steering. The near-field distribution in Figure 2(c3) shows that strong ED and MD are excited in the bigger and smaller rods, unlike Figure 2(b3), where most of the energy is confined in the bigger rods. More importantly, as shown in Figure 2(c2), CG2 takes EQs into the interference process. According to the generalized Kerker effect, the participation of EQs produces a highly directional scattering pattern, which cannot be approximated by the DA, as indicated in Figure 3(c3). Moreover, the R_0 and R_{-1} channels are eliminated well owing to the zero backward scattering. The totally symmetrical forward scattering cancels the T_0 channel and generates negative refraction with near-unity efficiency. Also, notice that the scattering pattern for the IL is very similar to that for a CG, but different from IR1 and IR2 (Figure S3b in the supplementary material). Therefore, the desired scattering pattern is mainly caused by the inter-lattice coupling, unlike CG1. The lattice coupling helps to optimize the scattering shape and further improves the working efficiency. Thus, we have demonstrated that the extra coupling inside the lattice increases the potential of the metagrating and excites high-order multipoles for the generalized Kerker effect.

To further show the promising ability of high-order multipoles, we present an extra example (CG3) with $r_1 = 1.3r$, $r_2 = 0.71r$, $\phi = 90°$, and $d = r_1 + r_2 + 0.08r$. Its working efficiency also exceeds 99%. The corresponding results are illustrated in Figure 2(d1)–(d4). In this case, the intriguing negative refraction is caused by the combination of the first four scattering modes. In contrast to the former designs, the high-order multipolar modes play a dominant role, as shown by the excited coefficients and far-field angular scattering patterns. From the near-field map of the lattice, we also see features of high-order multipoles. There are several zero points in the angular scattering pattern. Although CG3 has no-zero backward scattering, the directions of R_0 and R_{-1} coincide with the zero points. This is clear evidence that the high-order multipoles provide extra flexibility for the generalized Kerker effect, leading to the enhancement of working efficiency. Figure 2(d4) clearly indicates that the inter-lattice coupling is very important for forming the required scattering pattern. The lattice coupling is also necessary for the total suppression of unwanted diffraction channels. Therefore, by utilizing the coupling effect inside and among lattices, the high-order multipoles which are usually hard to control, can be excited efficiently and applied in wavefront engineering with impressive performances.

Next, we investigate the dependence of the in-plane negative refraction on the wavelength and the period of the grating, the results of which are plotted in Figure 3a and b, respectively. The theoretical calculations are accompanied

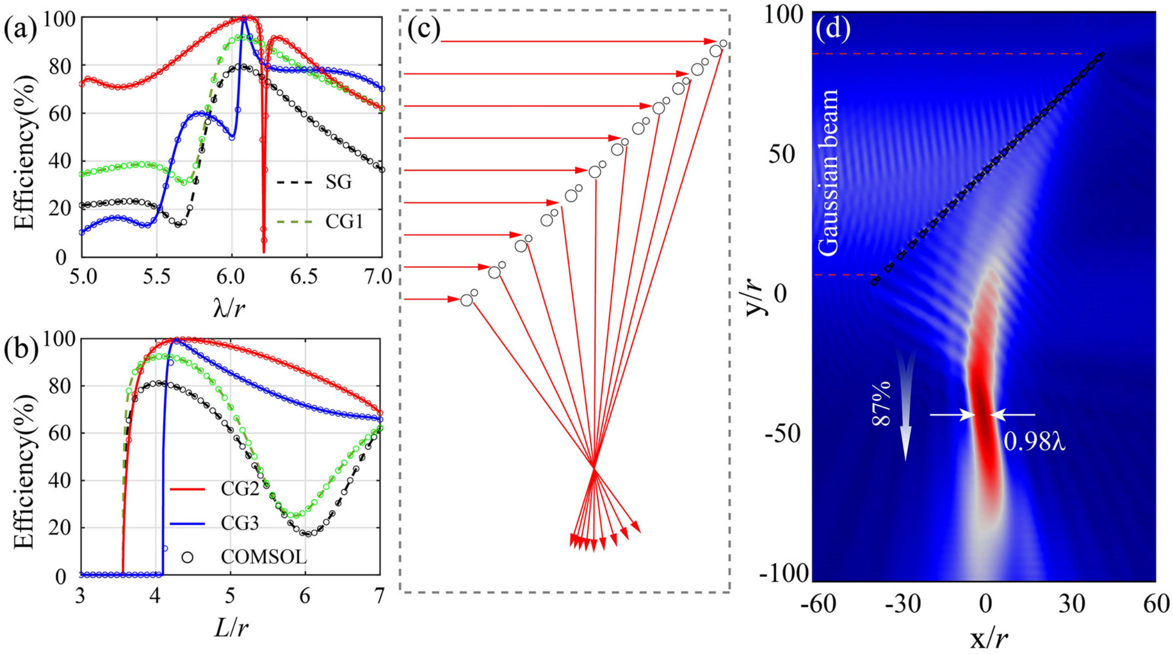

Figure 3: (a) and (b) efficiency of the negative refraction versus the working wavelength and period. The results calculated by COMSOL (circles) agree well with the theory; (c) schematic of the focusing of an incident wave by various rods; (d) field distribution of |*E*| when a Gaussian beam impinges on the designed grating, indicating that the focusing has 87% efficiency.

by the simulations performed by COMSOL Multiphysics. Periodic ports and boundaries are utilized in COMSOL for mimicking the incident plane wave and infinite metagratings. The theoretical results match the simulations well, verifying the validity of the theory. In Figure 3a, near the investigated wavelengths, Fano-shaped profiles can be recognized in the spectra of CG2 and CG3. The peaks and dips are associated with constructive and destructive interference between the dipoles and the high-order multipoles. This further indicates that the unity working efficiency is attributed to the participation of high-order multipoles. SG and CG1 have smooth wavelength responses because only dipoles are excited in both structures. In addition, the high efficiency of CG2 and CG3 is sustained over a large range of periods because the generalized Kerker effect for the two structures is mainly caused by the inter-lattice coupling. The variation of the period only has influences on the lattice coupling. As a comparison, SG and CG1 which are mainly based on the lattice coupling, have low tolerance with the change of period.

According to the above analysis for a metagrating, each value of the period is associated with a bending angle. Therefore, we can carefully modify the period to change the wavefront, thus achieving a complex wave control. As a specific realization, we designed a focusing lens. Its working schematic is illustrated in Figure 3c. According to the phase profile for focusing light [54], the period of the metagrating should be set as

$$L(x) = \frac{\lambda}{\frac{\sqrt{2}}{2} + |\cos(\Phi(x))|}, \tag{12}$$

where

$$\Phi(x) = \arcsin\left(\frac{\sqrt{2}}{2} \cdot \frac{f}{\sqrt{f^2 + x^2 + \sqrt{2}f|x|}}\right), \tag{13}$$

By setting a focal distance $f = 12\lambda$, we can get the distribution of period $L(x)$. After considering the value of local $L(x)$ and the global space of this metagrating, the position of each metaatom is obtained. The parameters of this focusing lens are put in Section 5 of the supplementary material, including the geometric size, phase response, and transmission coefficient of the metaatoms. The numerical simulation of a Gaussian beam impinging on the grating is presented in Figure 3d. The light is bent and focused to a specific position with an efficiency of over 85%. The full width at half maximum (FWHM) of the focusing point is about 0.98λ, as shown in Figure 3d. The focusing can be further optimized as Eqs. (12) and (13) do not consider the influence of the gradient period. The achieved result demonstrates the potential of these periodic nanoparticles. Of course, more applications based on this wavefront-shaping method are also possible.

The in-plane negative reflection means that the incident and reflected waves are on the same side of the normal. According to the above analysis, the waves scattered from the multipolar modes must undergo destructive interference with the incident waves in the 0th transmission channel and constructive interference in the −1st reflection channel. Moreover, the scattering due to specular reflection and −1st transmission should be suppressed. According to the generalized Kerker effect, the required angular scattering pattern cannot be achieved just by using the interaction between the MD and the ED.

An optimized SG for negative reflection is set as $L = 3.1r$ and $\lambda = \sqrt{2}L$. The simulated incident, scattering, and full-field waves are illustrated in Figure 4(a1)–(a3), respectively. Clearly, the radiating waves have a phase difference of π with the incident waves in the forward direction, whereas the backward scattering waves are in phase with the incoming waves. This scattering cancels out the incident waves and conserves the outgoing waves in the −1st reflection channel, leading to negative refraction with 89% efficiency. The scattering is mainly caused by the interference between the MD and the EQ, as indicated by the excited coefficients in Figure 4(a4). The features of the EQ can also be recognized in the insert of Figure 4(a3), which clearly shows the enhancement of the field induced. Compared with an IR, the lattice coupling increases the amplitude of the multipoles, fulfilling the generalized Kerker condition for negative reflection. The angular scattering pattern of this

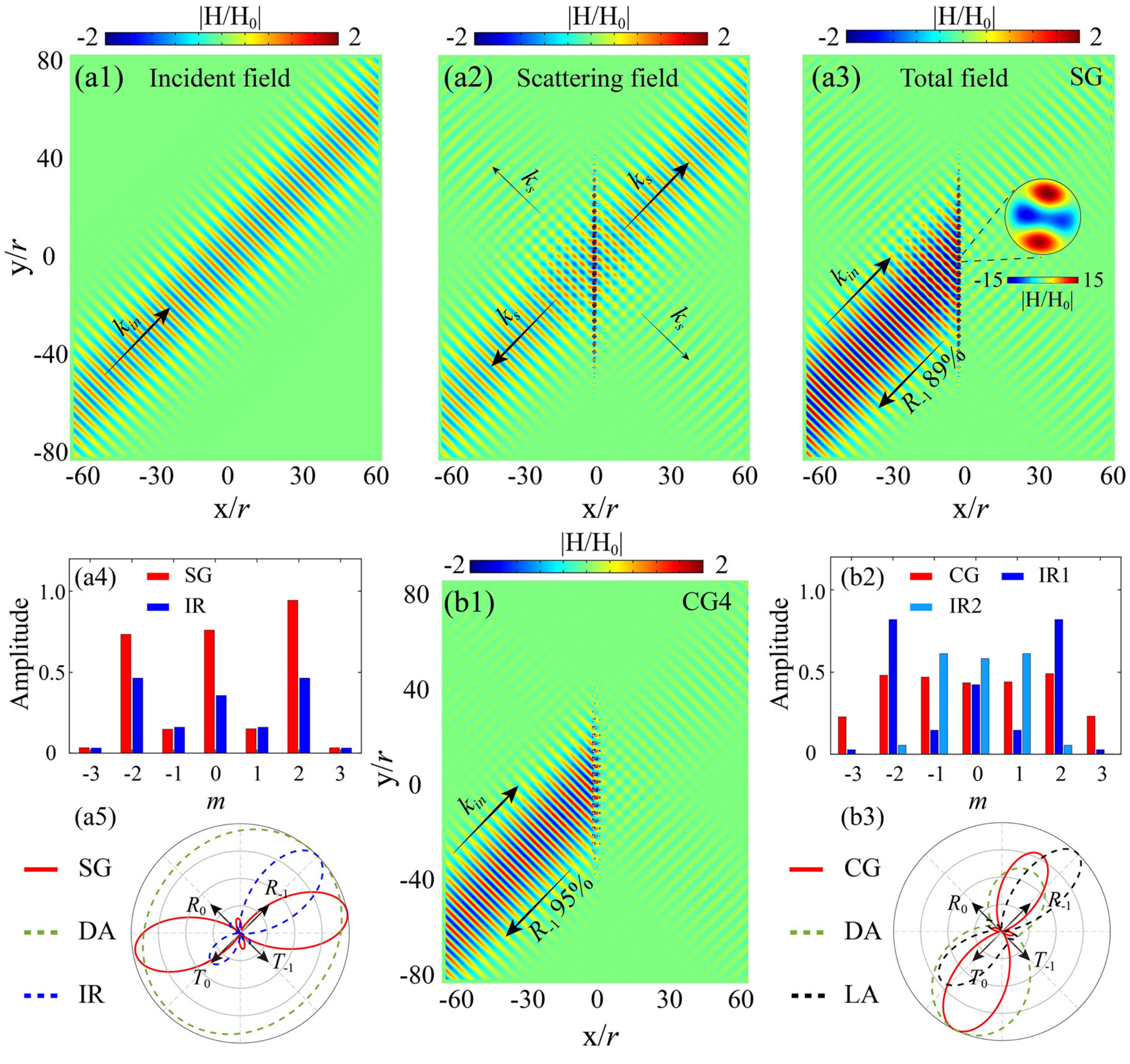

Figure 4: (a1)–(a3) depict the incident, scattering, and total field of H_z, respectively. The calculated SG with $L = 3.1r$ and $\lambda = \sqrt{2}L$; (a4) and (a5) coefficients of the excited multipoles and angular scattering patterns. (b1)–(b3) field map, coefficients of the multipoles, and the angular scattering patterns for CG4.

CG in Figure 4(a5) shows that the unwanted scattering channels are strongly suppressed, which cannot be realized by the DA or an IR. Optimized from the original SG, a CG (CG4) with $r_1 = 0.98r$, $r_2 = 0.62r$, $\phi = 0°$, $d = r_1 + r_2 + 0.54r$, and $L = 3.1r$ is calculated and the results are illustrated in Figure 4b. The working efficiency of CG4 reaches 95% because the R_0 and T_0 channels are further constrained by the additional rod. From the angular scattering patterns in Figure 4b and Figure S3d, it is clear that both the inter-lattice coupling and lattice coupling are important for fulfilling the generalized Kerker condition. Here, the first four multipoles are produced by the CG4 and contribute to wave manipulation. Compared with the SG, the dipoles in CG4 play a more important role and the high-order multipoles help to suppress unwanted channels, as indicated by the far-field angular scattering patterns.

The negative reflection of the chosen SG is very sensitive to the wavelength. The corresponding working bandwidth is of about 5%, as plotted in Figure 5a. These attributes to the properties of high-order multipoles are inherited in the negative refraction as the contribution of the ED is dominant. Due to the importance of lattice coupling and the high sensitivity of the ED, the working state strongly depends on the period of this grating, as shown in Figure 5b. These factors may create great challenges for practical fabrication. However, the high sensitivity of the working wavelength and geometry also offers significant potential for many applications [55], such as biomedical sensing, wavelength filtering, and hyperspectral imaging. As a specific example for use in a narrowband filter or multiplexer, the field distribution of this SG is put in Figure 5c whose calculated frequency is set as $\lambda = 4r$. More than 90% of the incident energy directly passes through the structure with little diffraction.

The performances of CG4 are similar to structures whose dipoles are dominant, as the high-order multipoles help to form the scattering pattern. Therefore, CG4 is tolerant to changes in the wavelength. The inter-lattice coupling also increases the stability with changes to the grating period. The slight deviation between theory and simulation when $L < 2.9r$ is caused by that the size of an IL $(r_1 + r_2 + d)$ is much larger than the period of grating L. In the deduction of the **T** matrix for CGs, the lattice is assumed as a composite structure. This assumption is inaccurate when the period is much smaller than the lattice. However, the trend of the theoretical curve is still well matched with the simulation in Figure 5b. By carefully tailoring the geometry, CG4 can be applied for complex wave steering. Figure 5d depicts an example by setting $L = 3.5r$. The angle of reflection is −53° for an efficiency of 85%. Therefore, the inter-lattice coupling is able to provide further potential for realizing the generalized Kerker effect and achieving high-efficient wave steering. In addition, the high-order multipoles can not only improve the working performance formed by dipoles but also dominantly achieve unique scattering patterns which are distinctive from dipoles.

4 Wave steering under TE polarization

In the following, we will show that the high-efficiency negative refraction and reflection realized for TM-polarized

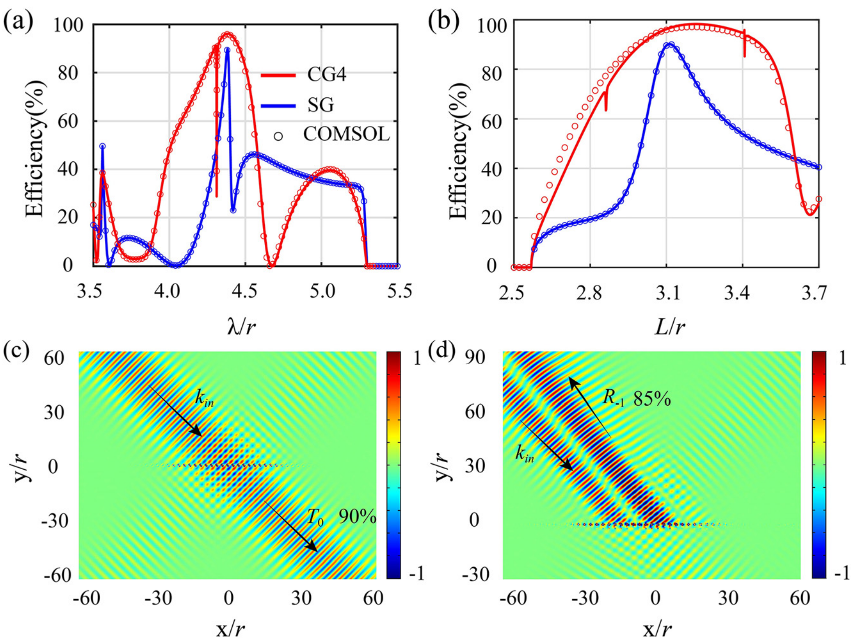

Figure 5: (a) and (b) Working efficiency of negative reflection versus the wavelength and the period of the gratings, respectively. The blue and red lines are the theoretical results for SG and CG4, respectively, whereas the circles are simulated results from COMSOL; (c) the field snapshot of SG when the calculated wavelength is $4r$, showing that most of the incident energy directly pass through the grating without any diffraction; (d) the reflection of CG4 with $L = 3.5r$.

waves are also achievable for TE polarization. As above, we first consider a CG with $L = 4.3r$ illuminated by 45° TE-polarized waves with $\lambda = \sqrt{2}L$. The field snapshot of the electric field is put in Figure 6(a1). The efficiency of the in-plane negative refraction is less than 50%. The two dipoles have coefficients like those for TM. The main difference is due to the strong excitation of the MQ mode, as shown in Figure 6(a2) and (a4). As indicated in Figure S1, the excited wavelengths of the multipoles for TE polarization are lower than those for TM polarization. Therefore, it is hard to get an ideal interference state with dipoles only. Then, we try to optimize the scattering pattern by adjusting the MQ. We calculated an optimized CG (CG5) with parameters $r_1 = r$, $r_2 = 0.22r$, $\phi = 90°$, $d = r_1 + r_2 + 0.05r$, and $L = 4.3r$. The field distribution of this CG is put in Figure 6(b1), indicating a working efficiency of 95%. The related multipolar excited coefficient, near-field distribution, and angular scattering patterns of the lattice are illustrated in Figure 6(b2)–(b4). From the calculated results, we can see that the improvement of the working efficiency can be attributed to the strong excitation of the MQ, due to the coupling inside the doublet. The MQ has great influences on the scattering pattern, leading to the canceling of two reflection channels, R_0 and R_{-1}, which cannot be achieved by the dipoles or an IR (see Figure S3e). Similar to CG1, the scattering properties of an IL are similar to IR1, indicating that the generalized Kerker effect is mainly caused by lattice coupling, whereas the inter-lattice coupling helps to excite high-order multipoles. To the best of our knowledge, this is the first reported efficient TE-polarized negative refraction based on dielectric metagratings because most previous studies considered only the contribution of dipoles.

Inspired by this result, we further explore the potential of the higher scattering mode MH using an SG with $r = 1.4r_1$ (r_1 is the same as for CG5) and $L = 3.06r$. The corresponding results are depicted in Figure 6(c1)–(c4), respectively. Negative refraction with efficiency of over 89% is obtained and the contribution of hexadecapole appears in the near-

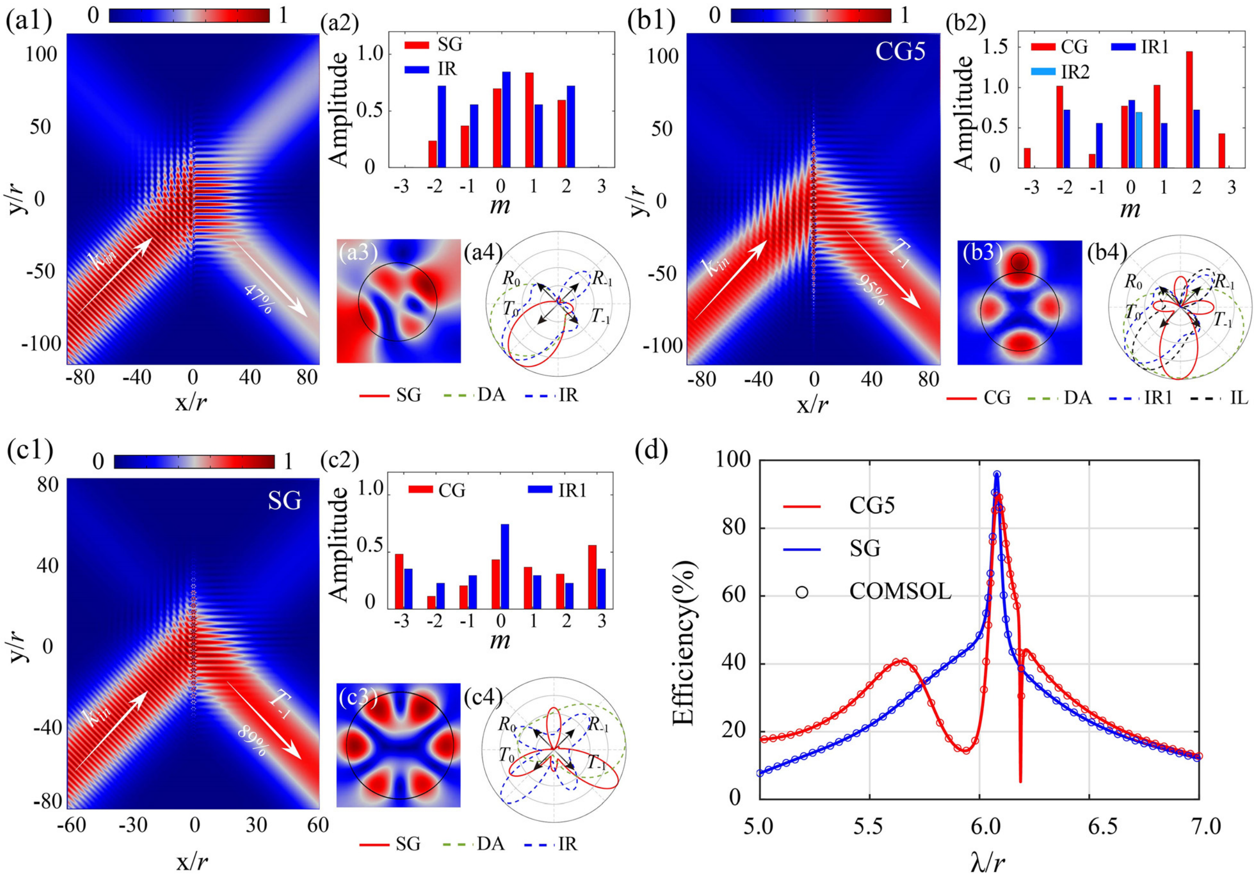

Figure 6: (a)–(c) calculated results of a reference SG with $L = 4.3r$, CG5, and an optimized SG, respectively. The numbers '1', '2', '3', and '4' are related to are respectively corresponding to the field distribution of $|E|$ when the rod array is illuminated by a Gaussian beam, the excited coefficients of the cylindrical harmonics, the near-field distribution of $|E|$ and the angular scattering patterns. The working wavelength is $\lambda = \sqrt{2}L$ and the incident angle is $\theta = 45°$, related to the negative refraction with a 90° bending angle; (d) is the working efficiency of CG5 and SG versus the calculated wavelength, accompanied by the simulated results by COMSOL.

field snapshot. Because of the multipole scattering and coupling, there are also significant excitation of ED, MD, and MQ, resulting in negative refraction through interference. The directions of the R_0 and R_{-1} channels coincide with the zero points in the angular scattering pattern. As above, the generalized Kerker condition cannot be fulfilled without the MH, fully verifying the necessity of the high-order multipoles. These designs clearly indicate that intriguing wave steering can be induced by the higher-order scattering multipoles. The working efficiency is plotted against the working wavelength in Figure 6d. Here, we emphasize that, although the quadrupole participates in the negative refraction for both TM and TE polarization, the situations are quite different. For the results in Figure 2c, the quadrupole is applied to enhance the working performance induced by the dipoles. For TE polarization, the quadrupole dominates the wave control. A similar conclusion is also valid for the MH in Figure 6c. Therefore, both structures have a high sensitivity to the working parameters. The relative working bandwidths are 7 and 6% for the wire gratings in Figure 6b and c.

Negative reflection is produced under TE polarization in the same way as for TM polarization, i.e., the high-order multipoles must be excited to realize the generalized Kerker effect. Based on this, two optimized CGs with $r_1 = 0.22r$, $r_2 = r$, $\phi = 90°$, $d = r_1 + r_2 + 0.05r$, and $L = 4.3r$ (CG6) and $r_1 = 0.42r$, $r_2 = 0.86r$, $\phi = 0°$, $d = r_1 + r_2 + 0.44r$, and $L = 4.3r$ (CG7) are chosen. Their efficiencies are respectively 92 and 94%. Interestingly, the parameters of CG6 are the same as those in Figure 6b, when the incident angle is set as 135°. The calculated results for this CG are shown in Figure 7(a1)–(a4) with $\theta = 45°$ and $\lambda = \sqrt{2}L$. As indicated in Figure 7(a3), the excited coefficient of MQ is much higher than other multipoles, fully verifying its importance. Compared with the negative refraction, the phase and amplitude of the multipoles for negative reflection have been changed owing to the variation of incident angle. The different interference states contribute to the different far-field scattering patterns, resulting in a transition between negative refraction and negative reflection. The calculated results for CG7 are shown in Figure 7(b1)–(b4). The features of the high-order multipoles have disappeared as the

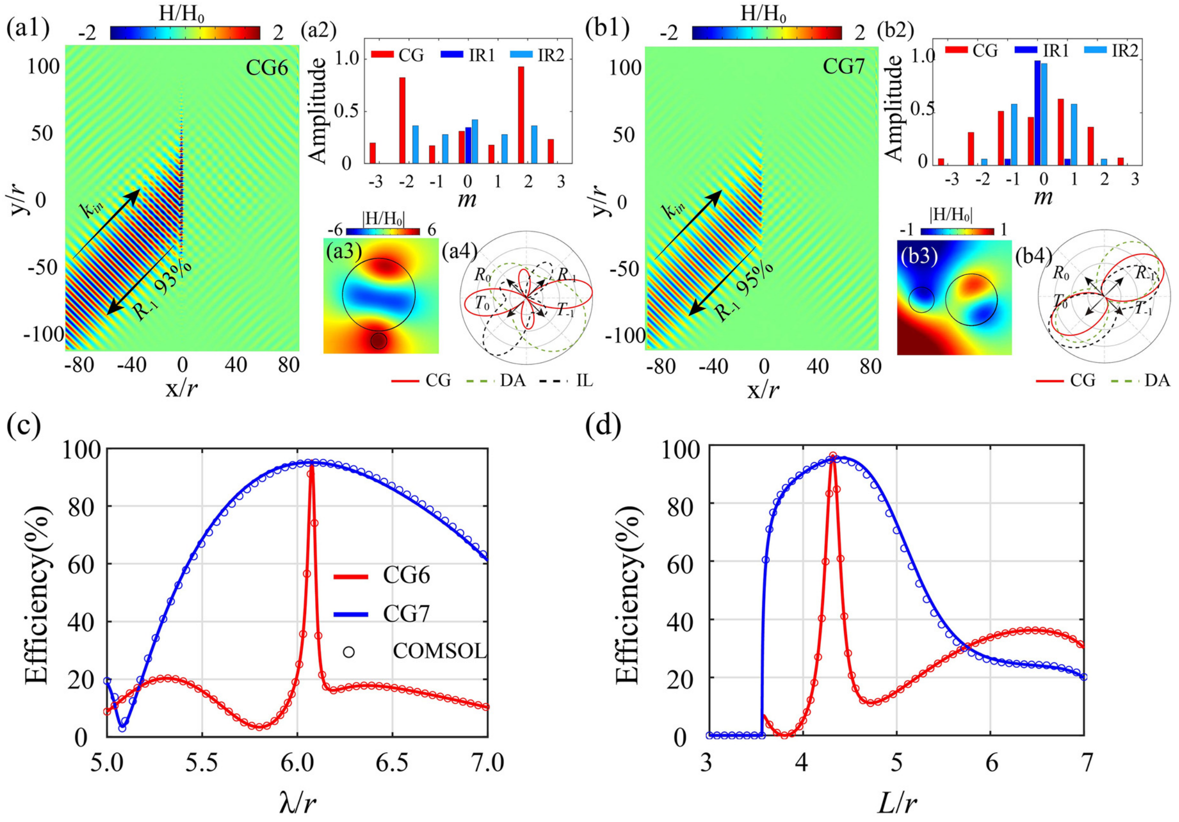

Figure 7: (a) and (b) show the calculated results of CG6 and CG7. The numbers ‘1’, ‘2’, ‘3’, and ‘4’ are respectively corresponding to the field distributions of E_z when the rod array is illuminated by a Gaussian beam, the excited coefficients of the cylindrical harmonics, the near-field distribution of $|E|$ and the angular scattering patterns. Other parameters are set as $\lambda = \sqrt{2}L$ and $\theta = 45°$; (c) and (d) are the working efficiency of CG6 and CG7 versus the working wavelength and the grating period, respectively.

dominant scattering modes have become dipoles. The MQ is still very important due to its ability to suppress the R_0 and T_{-1} channels, as indicated by the scattering patterns. The frequency responses are consistent with the former discussion. Owing to the contributions of high-order multipoles, CG7 is stable with the change of wavelength, whereas CG6 is very sensitive. The influences of changing period are highly dependent on the contributions of lattice coupling. For CG6, the scattering pattern of the IL approximation is like that for IR1, but different from the exact result. For CG7, both the inter-lattice coupling and lattice coupling are required for generating the desired angular scattering shape. Then, CG6 is more sensitive to the grating period than CG7.

5 Discussion and conclusion

Note that, although the promising wave steering is realized by using the metagrating profiles, the ability of dielectric rods is obviously not limited to the several functions demonstrated. Depending on the requirements, a rod grating can work in transmission or reflection mode and the working performance can be sensitive or robust to the parameters. The multipolar interference and collective lattice coupling provide flexible and complex wavefront control for TM and TE polarization. The working efficiency and fabrication demand of the dielectric rods can exceed the conventional gradient metasurfaces especially bending light with large angles. Note that, by using an asymmetrical CG, the abnormal control of waves with normal incidence is also realizable. We also present CG8, which has $r_1 = 0.9r$, $r_2 = 0.58r$, $\phi = 67°$, $d = r_1 + r_2 + 0.05r$, and $L = 7r$ and CG9, which has $r_1 = 0.81r$, $r_2 = 0.54r$, $\phi = 67°$, $d = r_1 + r_2 + r$, and $L = 7r$. These can achieve abnormal refraction of 50° for TM and TE polarization with $\theta = 90°$. The calculated wavelength is $L\,\sin(50°)$, leading to six diffraction channels: R_0, R_{-1}, R_1, T_0, T_1, and T_{-1}. The efficiencies achieved for the two structures are 92 and 90%, respectively, as shown in Figure 8a and b. For this design, the scattering patterns must have high directionality to suppress the four unwanted diffraction channels and cancel out the 0th transmission, which is more complex than previous investigations. From the far-field angular scattering patterns plotted in the insets, we can conclude that the backward scattering is suppressed well and the forward scattering is asymmetrical and highly directional, consistent with our predictions. The multiple couplings inside and among the lattice help to efficiently produce the first three multipoles, which lead to the required scattering properties.

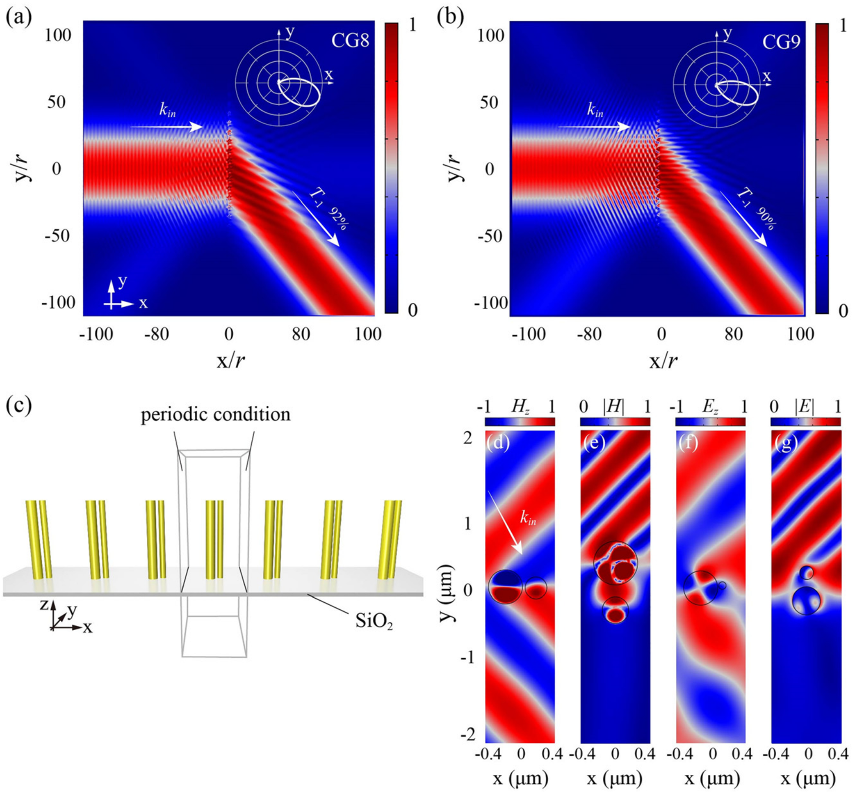

Figure 8: (a) and (b) calculated field maps of CG8 and CG9 under TM and TE polarization, respectively. The insets are the corresponding scattering patterns; (c) the scheme of the three-dimensional simulated model when the dielectric grating has a finite thickness; (d)–(g) the simulated field distributions of CG2, CG4, CG5, and CG7.

Considering practical fabrication, the metagratings must be truncated in the *z*-direction. Therefore, we performed serval full-wave 3D simulations to study the working performances of the metagratings. The height of the rods is set as 4 μm, located on silica (refractive index is 1.5) substrate with 300 nm thickness. The metagratings under these parameters are totally achievable through microfabrication, such as the E-beam lithography and the reactive ion etch [41, 43]. The configuration of the simulations is presented in Figure 8c, and more details are put in Section 6 of the supplement. Here, an individual lattice is chosen for calculation and periodic conditions are applied in the *x*-direction to mimic infinite gratings. Simulated results for CG2, CG4, CG5, and CG7 are illustrated in Figure 8d–g, respectively, corresponding to the negative refraction and reflection under both types of polarization. Further, other mentioned structures in Figures 2–8 are also calculated and put in the supplementary material. Clearly, the field maps in Figure 8 are fully consistent with the corresponding 2D results. Therefore, although the working properties of multipoles are influenced by the height of the rods [4], the high-efficiency wave steering can be achieved under realizable situations. The grating parameters can be further optimized to compensate for the finite thickness. In addition, the influence of loss in the infrared spectra is also investigated in detail (Section 7 of supplementary material). Although the working efficiency is slightly reduced, the unique scattering patterns due to interference among the multipoles are conserved when the loss is taken into account. In addition, compared with dipoles, the high-order multipoles are more sensitive to losses or the height of rods. For these designs (CG5 and CG6) which are mainly based on the high-order multipoles, the decrease of working efficiency is inevitable. There are still many challenges in efficiently applying the high-order multipoles.

In conclusion, in this work, we show that high-efficiency wave steering is achievable by the generalized Kerker effect which is based on interactions and coupling between multipole resonant modes of all-dielectric nanoparticles. Based on multipole scattering theory, both an SG formed by one rod per period and a CG formed by two rods per period are analyzed. The coupling inside and among the lattices can efficiently tailor the multipole states, leading to extensive scattering properties. By using the simple lattice configuration at the metagrating regime, high-efficiency negative refraction and reflection through large bending angles are demonstrated for both types of polarization. These effects are realized by controlling the diffraction channels through multipole interference. In addition to the fundamental dipoles, high-order multipoles with distinctive properties are studied and extensively applied for wave manipulation. These provide extra possibilities for nanoparticle-based beam control. This work may provide support for on-chip optical components, with functions such as bending, sensing, filtering, and focusing.

Supplement

The supplementary material is available for some supporting information. Section 1 investigates the scattering properties of cylindrical multipoles; In Section 2, we present the scattering properties of an isolated doublet; In Section 3, the **T** matrix for a CG is derived and the coupling inside the lattice is analyzed; Section 4 shows the scattering properties IRs in CG; Section 5 gives the parameters of the focusing lens; Section 6 describes the 3D simulations and some simulated results for the rods with a finite thickness; Section 7 investigates the influence of loss on the working performance.

Author contribution: All the authors have accepted responsibility for the entire content of this submitted manuscript and approved submission.

Research funding: The study was supported by the National Key Research and Development Program under Grant No. 2019YFA0210203 and the National Natural Science Foundation of China under Grant No. 61971013.

Conflict of interest: The authors declare no conflict of interest.

References

[1] T. J. Cui, D. R. Smith, and R. Liu, *Metamaterials*, Spring Street, NY, Springer, 2010.

[2] J. M. Hao, M. Qiu, and L. Zhou, "Manipulate light polarizations with metamaterials: from microwave to visible," *Front. Phys. China*, vol. 5, pp. 291–307, 2010.

[3] N. Yu, P. Genevet, M. A. Kats, et al., "Optically resonant dielectric nanostructures," *Science*, vol. 354, p. 6314, 2016.

[4] Y. H. Ko and R. Magnusson, "Wideband dielectric metamaterial reflectors: Mie scattering or leaky Bloch mode resonance?," *Optica*, vol. 5, pp. 289–294, 2018.

[5] I. Staude and J. Schilling, "Metamaterial-inspired silicon nanophotonics," *Nat. Photonics*, vol. 11, pp. 274–284, 2017.

[6] L. Zhou, X. Huang, Y. Zhang, et al., "Resonance properties of metallic ring systems," *Mater. Today*, vol. 12, pp. 52–59, 2009.

[7] E. Calandrini, A. Cerea, F. De Angelis, et al., "Magnetic hot-spot generation at optical frequencies: from plasmonic metamolecules to all-dielectric nanoclusters," *Nanophotonics*, vol. 8, pp. 45–62, 2018.

[8] Y. Yang, V. A. Zenin, and S. I. Bozhevolnyi, “Anapole-assisted strong field enhancement in individual all-dielectric nanostructures,” *ACS Photonics*, vol. 5, pp. 1960–1966, 2018.
[9] K. Koshelev, G. Favraud, A. Bogdanov, et al., “Nonradiating photonics with resonant dielectric nanostructures,” *Nanophotonics*, vol. 8, pp. 725–745, 2019.
[10] L. Carletti, A. Locatelli, D. Neshev, et al., “Shaping the radiation pattern of second-harmonic generation from AlGaAs dielectric nanoantennas,” *ACS Photonics*, vol. 3, pp. 1500–1507, 2016.
[11] D. A. Smirnova, A. B. Khanikaev, L. A. Smirnov, et al., “Multipolar third-harmonic generation driven by optically induced magnetic resonances,” *ACS Photonics*, vol. 3, pp. 1468–1476, 2016.
[12] B. Hopkins, D. S. Filonov, A. E. Miroshnichenko, et al., “Interplay of magnetic responses in all-dielectric oligomers to realize magnetic Fano resonances,” *ACS Photonics*, vol. 2, pp. 724–729, 2015.
[13] J. Yan, P. Liu, Z. Lin, et al., “Directional F‵ano resonance in a silicon nanosphere dimer,” *ACS Nano*, vol. 9, pp. 2968–2980, 2015.
[14] O. Yavas, M. Svedendahl, and R. Quidant, “Unravelling the role of electric and magnetic dipoles in biosensing with Si nanoresonators,” *ACS Nano*, vol. 13, pp. 4582–4588, 2019.
[15] R. M. Bakker, Y. F. Yu, R. Paniagua-Domínguez, et al., “Resonant light guiding along a chain of silicon nanoparticles,” *Nano Lett*, vol. 17, pp. 3458–3464, 2017.
[16] A. Krasnok, M. Caldarola, N. Bonod, et al., “Spectroscopy and biosensing with optically resonant dielectric nanostructures,” *Adv. Opt. Mater.*, vol. 6, 2018, Art no. 1701094.
[17] Z. Ma, S. M. Hanham, P. Albella, et al., “Terahertz all-dielectric magnetic mirror metasurfaces,” *ACS Photonics*, vol. 3, pp. 1010–1018, 2016.
[18] Y. H. Fu, A. I. Kuznetsov, A. E. Miroshnichenko, et al., “Directional visible light scattering by silicon nanoparticles,” *Nat. Commun.*, vol. 4, pp. 1–6, 2013.
[19] F. Todisco, R. Malureanu, C. Wolff, et al., “Magnetic and electric Mie-exciton polaritons in silicon nanodisks,” *Nanophotonics*, vol. 9, pp. 803–814, 2020.
[20] A. Furasova, E. Calabró, E. Lamanna, et al., “Resonant silicon nanoparticles for enhanced light harvesting in halide perovskite solar cells,” *Adv. Opt. Mater.*, vol. 6, 2018, Art no. 1800576.
[21] S. Xiao, J. Wang, F. Liu, et al., “Spin-dependent optics with metasurfaces,” *Nanophotonics*, vol. 6, pp. 215–234, 2017.
[22] O. Tsilipakos, A. C. Tasolamprou, T. Koschny, et al., “Pairing toroidal and magnetic dipole resonances in elliptic dielectric rod metasurfaces for reconfigurable wavefront manipulation in reflection,” *Adv. Opt. Mater.*, vol. 6, 2018, Art no. 1800633.
[23] A. Forouzmand and H. Mosallaei, “All-dielectric C-shaped nanoantennas for light manipulation: tailoring both magnetic and electric resonances to the desire,” *Adv. Opt. Mater.*, vol. 5, 2017, Art no. 1700147.
[24] J. Engelberg, C. Zhou, N. Mazurski, et al., “Near-IR wide-field-of-view Huygens metalens for outdoor imaging applications,” *Nanophotonics*, vol. 9, pp. 361–370, 2020.
[25] C. Liu, L. Chen, T. Wu, et al., “All-dielectric three-element transmissive Huygens’ metasurface performing anomalous refraction,” *Photon. Res.*, vol. 7, pp. 1501–1510, 2019.
[26] L. Zhang, J. Ding, H. Zheng, et al., “Ultra-thin high-efficiency mid-infrared transmissive Huygens meta-optics,” *Nat. Commun.*, vol. 9, p. 1481, 2018.
[27] M. I. Shalaev, J. Sun, A. Tsukernik, et al., “High-efficiency all-dielectric metasurfaces for ultracompact beam manipulation in transmission mode,” *Nano Lett*, vol. 15, pp. 6261–6266, 2015.
[28] S. M. Kamali, E. Arbabi, A. Arbabi, et al., “A review of dielectric optical metasurfaces for wavefront control,” *Nanophotonics*, vol. 7, pp. 1041–1068, 2018.
[29] J. Tian, Q. Li, P. A. Belov, et al., “High-Q all-dielectric metasurface: super and suppressed optical absorption,” *ACS Photonics*, vol. 7, pp. 1436–1443, 2020.
[30] S. Q. Li, W. Song, M. Ye, et al., “Generalized method of images and reflective color generation from ultrathin multipole resonators,” *ACS Photonics*, vol. 5, pp. 2374–2383, 2018.
[31] N. M. Estakhri and A. Alu, “Wave-front transformation with gradient metasurfaces,” *Phys. Rev. X*, vol. 6, 2016, Art no. 041008.
[32] A. Díaz-Rubio, V. S. Asadchy, A. Elsakka, et al., “From the generalized reflection law to the realization of perfect anomalous reflectors,” *Sci. Adv.*, vol. 3, 2017, Art no. e1602714.
[33] A. Epstein and G. V. Eleftheriades, “Synthesis of passive lossless metasurfaces using auxiliary fields for reflectionless beam splitting and perfect reflection,” *Phys. Rev. Lett.*, vol. 117, 2016, Art no. 256103.
[34] Y. Ra’di, D. L. Sounas, and A. Alù, “Metagratings: beyond the limits of graded metasurfaces for wave front control,” *Phys. Rev. Lett.*, vol. 119, 2017, Art no. 067404.
[35] E. Khaidarov, H. Hao, R. Paniagua-Domínguez, et al., “Asymmetric nanoantennas for ultrahigh angle broadband visible light bending,” *Nano Lett*, vol. 17, pp. 6267–6272, 2017.
[36] L. Z. Yin, T. J. Huang, F. Y. Han, et al., “Terahertz multichannel metasurfaces with sparse unit cells,” *Opt. Lett.*, vol. 44, pp. 1556–1559, 2019.
[37] X. Song, L. Huang, C. Tang, et al., “Selective diffraction with complex amplitude modulation by dielectric metasurfaces,” *Adv. Opt. Mater.*, vol. 6, 2018, Art no. 1701181.
[38] W. Liu and Y. S. Kivshar, “Generalized Kerker effects in nanophotonics and meta-optics,” *Opt. Express*, vol. 26, pp. 13085–13105, 2018.
[39] R. Paniagua-Dominguez, Y. F. Yu, E. Khaidarov, et al., “A metalens with a near-unity numerical aperture,” *Nano Lett*, vol. 18, pp. 2124–2132, 2018.
[40] D. Lin, M. Melli, E. Poliakov, et al., “Optical metasurfaces for high angle steering at visible wavelengths,” *Sci. Rep.*, vol. 7, pp. 1–8, 2017.
[41] J. Du, Z. Lin, S. T. Chui, et al., “Optical beam steering based on the symmetry of resonant modes of nanoparticles,” *Phys. Rev. Lett.*, vol. 106, 2011, Art no. 203903.
[42] H. Li, C. Qiu, J. Du, et al., “Broadband in-plane light bending with a doublet silicon nanopost array,” *IEEE Photon. J.*, vol. 8, pp. 1–5, 2015.
[43] A. Wu, H. Li, J. Du, et al., “Experimental demonstration of in-plane negative-angle refraction with an array of silicon nanoposts,” *Nano Lett*, vol. 15, pp. 2055–2060, 2015.
[44] H. Chalabi, Y. Ra’Di, D. L. Sounas, et al., “Efficient anomalous reflection through near-field interactions in metasurfaces,” *Phys. Rev. B*, vol. 96, 2017, Art no. 075432.
[45] V. E. Babicheva and A. B. Evlyukhin, “Resonant lattice Kerker effect in metasurfaces with electric and magnetic optical responses,” *Laser Photonics Rev*, vol. 11, 2017, Art no. 1700132.
[46] V. E. Babicheva and J. V. Moloney, “Lattice effect influence on the electric and magnetic dipole resonance overlap in a disk array,” *Nanophotonics*, vol. 7, pp. 1663–1668, 2018.
[47] W. Liu and A. E. Miroshnichenko, “Beam steering with dielectric metalattices,” *ACS Photonics*, vol. 5, pp. 1733–1741, 2017.

[48] H. Song, L. Sun, and G. P. Wang, “Tunable perfect magnetic mirrors and retroreflectors in terahertz band,” *Opt Express*, vol. 28, pp. 753–759, 2020.

[49] I. M. Hancu, A. G. Curto, M. Castro-López, et al., “Multipolar interference for directed light emission,” *Nano Lett*, vol. 14, pp. 166–171, 2014.

[50] W. Liu, “Generalized magnetic mirrors,” *Phys. Rev. Lett.*, vol. 119, 2017, Art no. 123902.

[51] P. D. Terekhov, A. B. Evlyukhin, D. Redka, et al., “Magnetic octupole response of dielectric quadrumers,” *Laser Photonics Rev*, vol. 14, 2020, Art no. 1900331.

[52] C. F. Bohren and D. R. Huffman, *Absorption and Scattering of Light by Small Particles*, Germany, John Wiley & Sons, 2008.

[53] K. Yasumoto and K. Yoshitomi, “Efficient calculation of lattice sums for free-space periodic Green’s function,” *IEEE Trans. Antenn. Propag.*, vol. 47, pp. 1050–1055, 1999.

[54] X. Yin, H. Zhu, H. Guo, et al., “Hyperbolic metamaterial devices for wavefront manipulation,” *Laser Photonics Rev*, vol. 13, 2019, Art no. 1800081.

[55] C. Yan, K. Y. Yang, and O. J. Martin, “Fano-resonance-assisted metasurface for color routing,” *Light Sci. Appl.*, vol. 6, p. e17017, 2017.

Supplementary Material: The online version of this article offers supplementary material (https://doi.org/10.1515/nanoph-2021-0158).